

Spatiotemporal pulse-shaping effects on 4-μm laser-driven Sn microdroplet plasmas for extreme ultraviolet emission

Qi Min(敏琦), Chunbo Miao(苗春波), Hongyu Liu(刘宏宇), Xingbang Liu(刘兴邦), Haidong Lu(卢海东), Maogen Su(苏茂根), and Chenzhong Dong(董晨钟)

Citation: Chin. Phys. B, 2026, 35 (**7**): 075203. DOI: 10.1088/1674-1056/ae74c1
http://cpb.iphy.ac.cn; http://iopscience.iop.org/cpb

What follows is a list of articles you may be interested in

Simulation on plasma discharge and transport in large and complex geometric space

Shiyi Tang(汤诗奕), Mengran Xiao(肖梦然), Ziqi Ma(马梓淇), Dongjie Yang(杨东杰), Xiaokai An(安小凯), Liangliang Liu(刘亮亮), Suihan Cui(崔岁寒), Ricky K. Y. Fu(傅劲裕), Paul K. Chu(朱剑豪), and Zhongzhen Wu(吴忠振)

Chin. Phys. B, 2026, 35 (**3**): 035202. DOI: 10.1088/1674-1056/adfebe

Optimization of an m = 0 multi-loop helicon source configuration for linear plasma devices: A comparative study with Boswell and half-helix antenna designs

Yi Yu(余羿), Hao Liu(刘灏), Xue-Dong Huang(黄学栋), Chen-Yu Xiao(肖晨雨), Lin Nie(聂林), Guang-Yi Zhao(赵光义), and Min Xu(许敏)

Chin. Phys. B, 2025, 34 (**12**): 125202. DOI: 10.1088/1674-1056/ade24b

New progress on DC H_2^+ beam generation: Tens of mA output and 70% fraction from a 2.45 GHz microwave driven ion source

Bujian Cui(崔步坚), Shixiang Peng(彭士香), Jianbin Zhu(朱建斌), Yicheng Dong(董宜承), Zhiyu Guo(郭之虞), and Jiaer Chen(陈佳洱)

Chin. Phys. B, 2025, 34 (**8**): 085203. DOI: 10.1088/1674-1056/adf1ec

Power transfer efficiency in an air-breathing radio frequency ion thruster

Gao-Huang Huang(黄高煌), Hong Li(李宏), Fei Gao(高飞), and You-Nian Wang(王友年)

Chin. Phys. B, 2024, 33 (**7**): 075201. DOI: 10.1088/1674-1056/ad426c

Transition from a filamentary mode to a diffuse one with varying distance from needle to stream of an argon plasma jet

Hui-Min Xu(许慧敏), Jing-Ge Gao(高敬格), Peng-Ying Jia(贾鹏英), Jun-Xia Ran(冉俊霞), Jun-Yu Chen(陈俊宇), and Jin-Mao Li(李金懋)

Chin. Phys. B, 2024, 33 (**1**): 015205. DOI: 10.1088/1674-1056/ad0149

Spatiotemporal pulse-shaping effects on 4-μm laser-driven Sn microdroplet plasmas for extreme ultraviolet emission

Qi Min(敏琦)[1,2,†], Chunbo Miao(苗春波)[1], Hongyu Liu(刘宏宇)[1], Xingbang Liu(刘兴邦)[1], Haidong Lu(卢海东)[1], Maogen Su(苏茂根)[1,2,‡], and Chenzhong Dong(董晨钟)[1,2,§]

[1] *Key Laboratory of Atomic and Molecular Physics & Functional Material of Gansu Province, College of Physics and Electronic Engineering, Northwest Normal University, Lanzhou* 730070, *China*

[2] *Gansu International Scientific and Technological Cooperation Base of Laser Plasma Spectroscopy, Lanzhou* 730070, *China*

(Received 3 April 2026; revised manuscript received 8 May 2026; accepted manuscript online 29 May 2026)

Drive lasers near the 4-μm wavelength offer a fundamental thermodynamic advantage for extreme ultraviolet (EUV) lithography by optimally balancing laser absorption and in-band EUV opacity. Using radiation-hydrodynamics simulations, we investigate spatiotemporal pulse-shaping effects on 4-μm-driven Sn microdroplet plasmas under an industrially relevant overfill geometry. An energy-conserved full-factorial strategy evaluates the independent influences of pulse duration, temporal envelope, and transverse spatial profile. Results reveal that temporal and spatial shaping govern distinct physical processes. Temporally, box-shaped profiles establish a quasi-steady-state hydrodynamic regime that sustains optimal ionization, preventing the severe over-ionization of high-peak Gaussian pulses and the under-heating of extended low-power pulses. Spatially, although transverse intensity variations negligibly impact macroscopic energy absorption, angular emission analyses demonstrate that flat-top beams uniformly ablate the target periphery. This suppresses the optically thick peripheral plasma shroud inherent to Gaussian beams, thereby minimizing angle-dependent self-absorption and enhancing isotropic EUV photon escape. Ultimately, combining a 15-ns box-shaped temporal envelope with a spatial flat-top profile achieves a maximum conversion efficiency of 3.35%. Thus, optimizing EUV emission requires utilizing temporal shaping to sustain intrinsic emissivity and spatial flattening to minimize radiation transport losses.

Keywords: laser-produced tin plasma, extreme ultraviolet lithography, 4-μm nanosecond laser, radiation-hydrodynamics simulation

PACS: 52.50.Dg, 52.20.–j, 52.25.–b, 52.25.Os, 52.65.–y

DOI: 10.1088/1674-1056/ae74c1 **CSTR:** 32038.14.CPB.ae74c1

1. Introduction

Extreme ultraviolet (EUV) lithography operates at 13.5 nm, where projection optics are built around the narrow reflectance band of Mo/Si multilayer mirrors, and has become the key exposure technology for the most advanced integrated circuits.[1–5] In current source architectures, the required radiation is generated from laser-produced tin (Sn) plasmas, because multiply charged Sn ions (predominantly Sn^{10+} to Sn^{14+}) emit strongly near 13.5 nm.[1–5] However, efficiently extracting these photons from a highly dynamic and opaque plasma environment to meet the massive power demands of modern scanners remains a formidable task. The central challenge is therefore not simply the production of intense EUV radiation, but the generation of high in-band power with favorable conversion efficiency (CE), spectral purity, source size, and angular characteristics under lithography-relevant conditions.[3,4]

State-of-the-art industrial EUV sources are based on molten Sn microdroplets[6] irradiated in a dual-pulse scheme, in which a prepulse first reshapes the droplet and a more energetic main pulse subsequently generates the EUV-emitting plasma.[3,4] In practice, the commercial route relies on 10.6-μm CO_2 laser drivers, which have enabled high-volume-manufacturing source performance. However, this approach is accompanied by complex target preparation and massive facility footprints. Consequently, solid-state drivers remain highly attractive because of their potential advantages in compactness, scalability, and wall-plug efficiency.[7] These considerations have motivated sustained interest in shorter-wavelength solid-state and mid-infrared laser drivers as candidate routes for future EUV source development.[7–17]

Among the alternative driver wavelengths, the 1–2 μm range has already demonstrated that moving away from the conventional CO_2 regime can substantially reshape the plasma conditions relevant to EUV generation.[7–17] Schupp *et al.* experimentally showed that 1- and 2-μm-wavelength laser-driven Sn microdroplet plasmas can exhibit similar spectral features when the required drive intensity scales approximately as λ^{-1}, while the 2-μm case benefits from distinctly improved spectral performance associated with lower-density

†Corresponding author. E-mail: mq_lpps@nwnu.edu.cn
‡Corresponding author. E-mail: sumg@nwnu.edu.cn
§Corresponding author. E-mail: dongcz@nwnu.edu.cn

© 2026 Chinese Physical Society and IOP Publishing Ltd. All rights, including for text and data mining, AI training, and similar technologies, are reserved.

plasma conditions and reduced optical-depth effects.[14] More recently, Mostafa *et al.* reported in-band CEs up to 5.0% from 2-μm laser-driven Sn microdroplet plasmas by achieving sufficiently homogeneous plasma heating through optimization of pulse duration, spot size, and the temporal and spatial properties of the drive pulse.[10] Together, these studies make clear that source performance is governed not by wavelength alone, but by the spatiotemporal manner in which laser energy is deposited into the target plasma.

The broader wavelength dependence of Sn-based EUV source performance has been clarified further by recent radiation-hydrodynamic simulations. Hemminga *et al.* systematically characterized laser-driven Sn microdroplet plasmas over the wavelength range 1.064–10.6 μm and showed that the existence of a CE maximum near 4 μm originates from the interplay between the optical depth of the incident laser light and that of the in-band EUV photons for a given droplet geometry.[8] This result places 4 μm in a physically distinguished regime; it corresponds to a thermodynamic "sweet spot" in which laser coupling and in-band reabsorption can become favorably balanced. Very recent simulations on preformed Sn targets further reinforced the importance of this wavelength region, reporting CE values up to 7.1% under 4-μm irradiation when long-pulse and spatially uniform heating conditions are established.[18]

From the laser-technology perspective, 4 μm drivers have also attracted increasing attention in the broader development of mid-infrared laser sources. Solid-state and nonlinear-conversion schemes, including optical parametric sources based on $ZnGeP_2$ crystals, have demonstrated access to high-power nanosecond radiation in this wavelength region.[19] However, compared with the mature 10.6 μm-CO_2-laser systems used in present industrial EUV sources, practical 4 μm drivers still face challenges in pulse energy, average power, repetition rate, long-term stability, beam control, and overall system robustness. Thus, 4 μm laser-driven Sn plasma sources should presently be regarded as an emerging and exploratory route rather than an established industrial technology. This situation makes numerical studies particularly useful for evaluating the source-physics potential of this wavelength before full laser-system maturity is reached. Once a favorable wavelength regime is identified, the next key question is how the laser energy should be delivered in time and across the focal spot to fully exploit this wavelength advantage.

Concurrently, a substantial body of work has shown that pulse shaping can be as important as wavelength selection. Early studies already identified optical depth, pulse duration, focal spot size, and laser wavelength as key parameters governing the in-band output of Sn plasmas.[20–23] More recently, Sizyuk *et al.* showed that temporal prepulse shaping in a dual-pulse tin-microdroplet system can increase the EUV output by 24% relative to a standard Gaussian prepulse at the same pulse energy.[24] On the spatial side, Dong *et al.* demonstrated that tailoring the transverse laser profile for preformed Sn disk targets can raise the CE from 3.5% to 4.1% under otherwise identical irradiation conditions.[25] These results strongly suggest that the laser waveform should be regarded as a primary control parameter of EUV-source physics rather than as a secondary technical detail.

Despite these advances, an important gap remains in the open literature. Existing studies have largely focused on wavelength optimization, prepulse design, or profile tailoring in dual-pulse or preformed-target configurations, whereas controlled single-pulse comparisons at a fixed 4-μm wavelength under identical droplet, focusing, and energy conditions remain limited. This gap is significant because the physical origin of the favorable 4-μm regime itself is a balance between absorption and opacity, and that balance is expected to depend sensitively on how the laser energy is distributed in time and across the focal spot. To the best of our knowledge, a fully balanced study that separately resolves the roles of pulse duration, temporal envelope, and transverse intensity profile for Sn microdroplet plasmas driven by a 4-μm laser has not yet been systematically reported in the open literature. This unresolved issue directly motivates the present work.

In this work, we perform a factor-resolved comparative study of Sn microdroplet plasmas driven by a 4-μm nanosecond laser by independently varying three factors: pulse duration, temporal waveform, and transverse intensity profile. Specifically, we adopt a fully balanced $2 \times 2 \times 2$ design comprising two pulse durations (15 ns vs. 36 ns), two temporal envelopes (box-shaped vs. Gaussian), and two spatial beam profiles (flat-top vs. Gaussian), while keeping the laser wavelength, total pulse energy, focal size, droplet radius, and initial density fixed. This design enables us to disentangle the main and coupled effects of spatiotemporal pulse shaping on the distributions of plasma state parameters and to correlate these changes directly with the resulting EUV radiation metrics, such as in-band CE. Ultimately, this study establishes a comprehensive physical framework detailing how temporal waveform control sustains the optimal transient ionization balance and how spatial profile flattening mitigates peripheral opacity to minimize angle-dependent radiation transport losses in mid-infrared-driven extreme ultraviolet sources.

2. Numerical model and simulation setup

We performed numerical simulations of laser-produced Sn plasmas using the two-dimensional radiation-hydrodynamics code RHDLPP,[26,27] together with its three-dimensional spectral post-processing module SpeIma3D.[26–30] The integrated RHDLPP–SpeIma3D framework enables self-consistent prediction of plasma evolution

and detector-relevant EUV observables, and has been applied previously to the investigation of LPP dynamics and EUV emission in parameter regimes relevant to lithographic light sources.[26,27,31,32] In the following, we briefly summarize the numerical model and specify the simulation setup adopted in the present work.

2.1. Numerical model

RHDLPP is a flux-limited multigroup radiation-hydrodynamics code developed for the simulation of laser-produced plasmas. The governing equations are solved in an Eulerian framework and can be configured in one- or two-dimensional Cartesian, cylindrical, or spherical geometries. RHDLPP incorporates the principal physical modules required for Sn-plasma EUV-source simulations, including hydrodynamics, electron heat conduction, multigroup radiation transport, laser propagation and energy deposition, equation of state, ionization-state calculation, and spectral synthesis. Radiation transport is treated using a multigroup flux-limited diffusion approximation. The coupled hyperbolic-parabolic system is advanced by an operator-splitting strategy: the hyperbolic subsystem associated with fluid motion and radiation advection is solved explicitly, whereas the stiff parabolic subsystem, including radiation diffusion, heat conduction, and energy exchange, is treated implicitly to ensure numerical stability and robustness.

Laser propagation and energy deposition are modeled using a hybrid approach that combines geometrical-optics ray tracing in subcritical plasma regions with a one-dimensional solution of the Helmholtz wave equation in supercritical regions, allowing broadband simulations over a wide range of laser wavelengths. Thermodynamic quantities are evaluated using a quotidian equation of state (QEOS). Charge-state distributions and average ionization levels are obtained from a steady-state collisional-radiative model based on screened-hydrogenic atomic data.

To obtain detector-relevant EUV observables from the strongly nonuniform and optically thick Sn plasmas, we employ the post-processing module SpeIma3D. This module reconstructs a three-dimensional plasma volume by revolving the two-dimensional axisymmetric (r, z) fields about the symmetry axis, and then performs detector-consistent ray tracing through the reconstructed plasma. Along each ray, the local wavelength-dependent emissivity and absorption coefficient are evaluated from the plasma state, and the radiative transfer equation is solved to obtain the emergent spectral intensity. By integrating over the accepted ray ensemble, detector area, and time, SpeIma3D yields time-resolved and time-integrated spectra, angle-dependent spectra, transient images, and derived quantities such as the in-band energy, CE, and SP.

Further details regarding the numerical formulation, implementation, verification, and representative applications of RHDLPP and SpeIma3D have been reported in our previous publications[26–31] and are not repeated here.

2.2. Simulation setup

In the present study, all simulations are performed for a spherical liquid Sn microdroplet with radius $R_0 = 23$ μm and initial density $\rho_0 = 6.9$ g/cm^3. The incident laser wavelength is fixed at 4 μm, the total laser energy is fixed at 77 mJ, and the focal-spot radius is fixed at 54 μm. The value of 77 mJ was selected so that the reference irradiation condition, namely the 15 ns box-shaped pulse with a 54 μm radius flat-top beam, corresponds to an average laser intensity of approximately 0.56×10^{11} W/cm^2, which lies near the favorable 4 μm operating regime identified in the wavelength–intensity scan discussed below. Keeping the total laser energy fixed for all cases also ensures that the subsequent comparison isolates the effects of pulse duration, temporal waveform, and transverse intensity profile, rather than changes in the total input-energy scale.

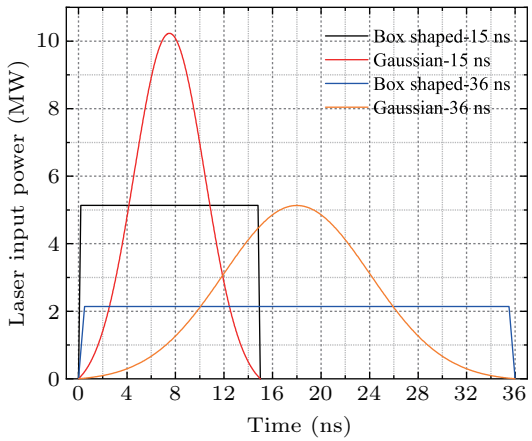


Fig. 1. Temporal laser input-power waveforms adopted in this work. Four representative temporal cases are considered: 15 ns box-shaped (black), 15 ns Gaussian (red), 36 ns box-shaped (blue), and 36 ns Gaussian (orange) pulses.

To this end, we adopt a fully balanced $2 \times 2 \times 2$ design comprising two pulse durations, two temporal waveforms, and two spatial profiles. The pulse durations are 15 ns and 36 ns. The 15 ns duration was chosen as the reference nanosecond pulse width for the present 4 μm irradiation condition, because this timescale is commonly used in Nd:YAG-driven Sn microdroplet EUV studies; for example, Schupp *et al.*[9] employed 15 ns temporally shaped pulses with a flat-top spatial profile in their experimental study of EUV generation from Sn microdroplet plasmas. The 36 ns duration was introduced as an extended-pulse case to examine how slower energy delivery affects plasma heating, hydrodynamic expansion, ionization balance, and EUV emission under the same total laser energy. For each duration, the temporal waveform is taken to be ei-

ther box-shaped or Gaussian. The corresponding laser input-power histories are shown in Fig. 1. To strictly conserve the total pulse energy of 77 mJ, the power amplitudes are mathematically scaled as follows: for the 15-ns box-shaped pulse, the laser power is constant at 5.13 MW; for the 15-ns Gaussian pulse, the temporal full width at half maximum (FWHM) is 7 ns, the peak-power time is 7.7 ns, and the peak power is 10.23 MW; for the 36-ns box-shaped pulse, the laser power is constant at 2.14 MW; and for the 36-ns Gaussian pulse, the temporal FWHM is 14.3 ns, the peak-power time is 18 ns, and the peak power is 5.13 MW.

For the transverse intensity distribution, two spatial profiles are considered. The first is a flat-top profile with a beam radius of 54 μm. The second is a Gaussian profile with a transverse FWHM of 66 μm. Since the 23 μm radius Sn microdroplet has an initial diameter of 46 μm, the characteristic transverse size of the laser focal spot is larger than the initial droplet size for both spatial profiles. We refer to this irradiation configuration as the overfill geometry. By combining the four temporal cases shown in Fig. 1 with the two spatial profiles, a total of eight irradiation conditions are constructed. The complete set of simulated cases is summarized in Table 1.

Unless otherwise specified, the in-band CE is defined as the ratio of the time-integrated EUV energy within 13.5 nm ±1% emitted into the full collector-side hemisphere to the total incident laser energy. The collection solid angle used for the CE calculation is 2π steradians.

Table 1. Laser conditions for the eight simulated cases.

Case	Pulse duration (ns)	Temporal waveform	Spatial profile
1	15	Box-shaped	Flat-top (radius = 54 μm)
2	15	Box-shaped	Gaussian (FWHM = 66 μm)
3	15	Gaussian (FWHM = 7 ns)	Flat-top (radius = 54 μm)
4	15	Gaussian (FWHM = 7 ns)	Gaussian (FWHM = 66 μm)
5	36	Box-shaped	Flat-top (radius = 54 μm)
6	36	Box-shaped	Gaussian (FWHM = 66 μm)
7	36	Gaussian (FWHM = 14.3 ns)	Flat-top (radius = 54 μm)
8	36	Gaussian (FWHM = 14.3 ns)	Gaussian (FWHM = 66 μm)

3. Results and discussion

Before discussing the waveform dependence of the eight simulated cases, we first clarify the motivation for selecting a 4-μm driver wavelength. Figure 2 shows the calculated CE as a function of laser wavelength and laser intensity for Sn microdroplets under the common reference irradiation condition defined by case 1 in Section 2. As visualized by the bubble sizes in Fig. 2, the CE exhibits a pronounced, non-monotonic dependence on the drive wavelength. At shorter wavelengths (e.g., 1.064 μm), the inherently high critical electron density ($n_c \propto \lambda^{-2}$) generates an optically thick plasma corona. Consequently, the generated 13.5-nm EUV photons undergo severe reabsorption before escaping the plasma, which limits the achievable CE. Conversely, at 10.6 μm, although the plasma is optically thin to EUV radiation, the low critical density reduces the inverse bremsstrahlung absorption efficiency, leading to suboptimal laser–plasma coupling. A macroscopic thermodynamic optimum emerges in the mid-infrared regime. Specifically, the 4-μm driver establishes a condition where the plasma ($n_c \approx 6.25 \times 10^{19}$ cm^{-3}) is sufficiently dense to absorb the incident laser energy efficiently, yet adequately rarefied to permit the escape of in-band photons, yielding a maximum CE exceeding 3.3%. This fundamental wavelength advantage justifies anchoring the drive wavelength at 4 μm, ensuring that the subsequent CE variations are exclusively attributable to spatiotemporal hydrodynamic manipulation.

It should be emphasized that Fig. 2 is used here to justify the choice of 4 μm as the driver wavelength, not to claim a universally optimal wavelength for all pulse shapes. Rather, it shows that 4 μm already provides a highly competitive operating window under a common reference waveform, making it an appropriate wavelength at which to isolate the effects of pulse duration, temporal waveform, and transverse profile.

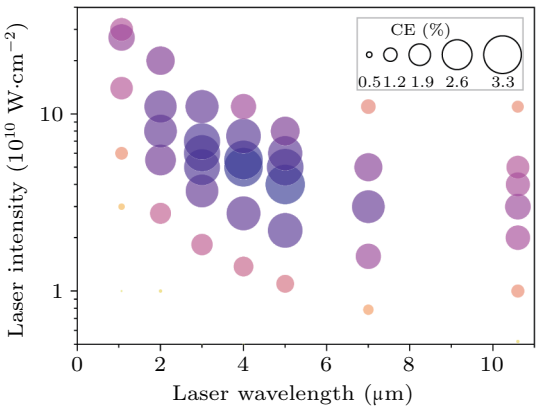


Fig. 2. Calculated in-band EUV CE as a function of the drive laser wavelength and peak laser intensity. The area of each circular marker is proportional to the calculated CE value, with a reference scale provided in the inset. All data points in this parameter scan utilize the spatiotemporal irradiation configuration of case 1 (a 15-ns box-shaped temporal profile and a 54-μm-radius flat-top spatial profile) irradiating an identical 23-μm-radius spherical liquid Sn droplet.

With the wavelength fixed at 4 μm and the total single-pulse energy strictly conserved at 77 mJ, the influence of spatiotemporal waveforms on the dynamic coupling of laser en-

ergy into the target is investigated. Figure 3 illustrates the temporal evolution of the prescribed incident laser power (smooth envelope curves) and the calculated absorbed power (fluctuating curves) for the eight cases. For clarity, the case numbers used in Figs. 3–7 follow the irradiation conditions defined in Table 1. The high-frequency fluctuations in the absorbed power reflect the dynamic interaction between the continuous hydrodynamic expansion of the plasma and the laser ray-tracing absorption process.

A primary observation from Fig. 3 is the distinct transition between transient and quasi-steady-state absorption behaviors governed by the temporal pulse shape. For the box-shaped temporal profiles (cases 1, 2, 5, and 6), the absorbed power exhibits a rapid initial rise during the first few nanoseconds, followed by a prolonged, stable plateau. During this plateau, the absorbed power fluctuates around a nearly constant mean value (approximately 4.0 MW for cases 1 and 2, and 1.9 MW for cases 5 and 6) until the termination of the pulse. This behavior indicates that a quasi-steady-state hydrodynamic regime is established, where laser energy deposition dynamically balances the energy dissipation through plasma expansion. In contrast, for the Gaussian temporal profiles (cases 3, 4, 7, and 8), the absorbed power continuously tracks the transient rising and falling edges of the incident pulse, retaining the overarching Gaussian characteristic without forming a steady-state absorption phase.

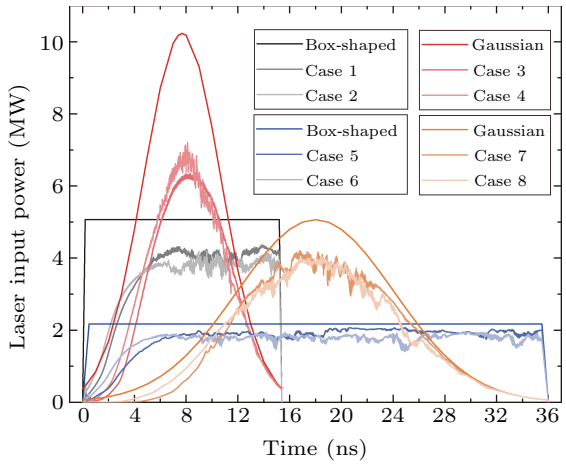


Fig. 3. Temporal evolution of the prescribed incident laser power (smooth envelope curves) and the dynamically calculated absorbed power (fluctuating curves) for the eight spatiotemporal configurations. The incident drive wavelength is fixed at 4 μm. Within each temporal waveform pairing, configurations employing a spatial flat-top profile (cases 1, 3, 5, and 7) are denoted by darker lines, while those utilizing a spatial Gaussian profile (cases 2, 4, 6, and 8) are denoted by lighter lines. The case numbers correspond to the irradiation conditions summarized in Table 1.

Furthermore, Fig. 3 reveals that the macroscopic absorbed power is relatively insensitive to the transverse spatial profile under the evaluated overfill geometry. Within each temporal waveform pairing, the fluctuating absorbed power curves for the spatial flat-top configurations (e.g., cases 1, 3, 5, and 7) and their spatial Gaussian counterparts (e.g., cases 2, 4, 6, and 8) largely overlap, exhibiting no substantial systematic difference in magnitude. This indicates that modifying the transverse intensity distribution from a Gaussian to a flat-top profile under these specific conditions does not drastically alter the total fraction of laser energy coupled into the expanding plasma. Additionally, the data demonstrate that the instantaneous absorption fraction depends heavily on the incident power level. For the low-power 36-ns box-shaped pulses (cases 5 and 6, maintained at 2.14 MW), the absorbed power curves closely approach the incident power envelopes, representing a highly efficient macroscopic fractional absorption. However, for the 15-ns Gaussian pulses (cases 3 and 4), which introduce a high peak power of 10.23 MW, a substantial absolute difference emerges between the incident and absorbed power near the pulse peak. The maximum absorbed power saturates near 6.5 MW, indicating a notable decrease in the absorption fraction. This suggests that at extreme intensities, a larger portion of the incident laser energy is decoupled from the target, likely due to enhanced reflection or refraction at the critically dense surface before it can be absorbed.

The spatiotemporal distribution of this absorbed energy fundamentally determines the thermodynamic states and the resulting EUV emissivity. Efficient 13.5-nm emission requires a substantial volume of the Sn plasma to be maintained within an electron temperature (T_e) range of 30–40 eV, which predominantly populates the EUV-emitting Sn^{10+} to Sn^{14+} ion stages. Figure 4 presents the two-dimensional spatial distributions of T_e and the average charge state (Z_{ave}) for all eight cases. To ensure a thermodynamically equivalent comparison independent of the total pulse duration, these spatial profiles are extracted at the temporal midpoint of the cumulative energy deposition, corresponding to the time when exactly 38.5 mJ of laser energy has been delivered ($t = 7.5$ ns for the 15-ns pulses, and $t = 18.0$ ns for the 36-ns pulses). The black circle marks the initial droplet, and the brown contour indicates the critical-density surface for the 4-μm laser.

The distributions in Fig. 4 illustrate that the transverse spatial profile of the laser exerts a negligible influence on the macroscopic plasma morphology under the evaluated overfill conditions. A direct comparison between the spatial flat-top configurations (left column) and their spatial Gaussian counterparts (right column) for any given temporal waveform reveals that the geometric contours of the critical density surfaces and the spatial extents of the high-temperature and highly ionized regions are visually indistinguishable. Because the characteristic transverse dimensions of the laser focal spots (54 μm radius and 66 μm FWHM) significantly exceed the 46–μm initial droplet diameter, the spherical target interacts predominantly with the central, relatively uniform portion of the incident beam. Consequently, the local ablative pressure gradients established across the droplet surface remain com-

parable regardless of the overarching transverse intensity distribution, leading to similar multidimensional hydrodynamic expansion dynamics. This spatial insensitivity corroborates the comparable macroscopic absorption behaviors observed in Fig. 3.

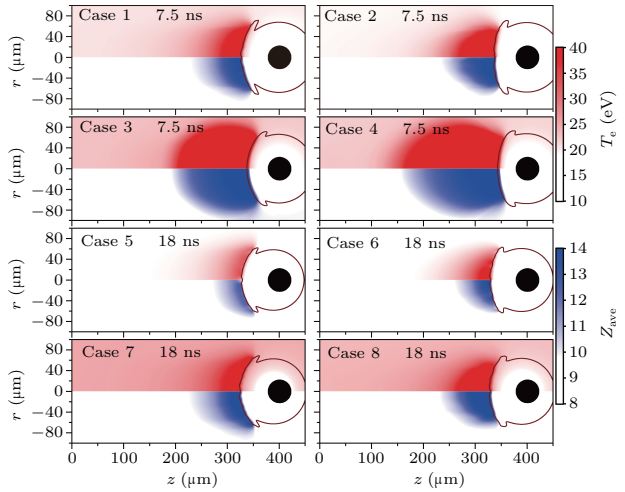


Fig. 4. Two-dimensional axisymmetric spatial distributions of the electron temperature (T_e, upper halves) and the average charge state (Z_{ave}, lower halves) on the r–z plane for the eight spatiotemporal configurations. The solid black circles indicate the initial size and position of the 23-μm-radius Sn droplet. The solid brown curves delineate the dynamically expanding critical electron density surface for the 4-μm drive laser ($n_c \approx 6.25 \times 10^{19}$ cm^{-3}). To ensure a thermodynamically equivalent comparison independent of the total pulse duration, the spatial fields are extracted at the temporal midpoint of the cumulative energy deposition, corresponding to exactly 38.5 mJ of delivered laser energy ($t = 7.5$ ns for the 15-ns pulses and $t = 18.0$ ns for the 36-ns pulses). The case numbers correspond to the irradiation conditions summarized in Table 1.

Given this macroscopic spatial similarity, Fig. 4 demonstrates that the ionization balance and the thermodynamic trajectories are overwhelmingly dictated by the temporal power injection rate. For the 15-ns Gaussian profiles (cases 3 and 4), the high peak power of 10.23 MW rapidly heats the plasma corona. The localized T_e readily exceeds 40 eV, driving the ionization state beyond the optimal stages ($Z_{ave} > 14$). This excessive ionization depletes the primary EUV-emitting Sn ions, redirecting absorbed energy into out-of-band transitions. Conversely, the 36-ns box-shaped profiles (cases 5 and 6) provide a protracted energy injection rate of 2.14 MW. This low power is insufficient to overcome continuous hydrodynamic expansion cooling, resulting in a plasma that remains under-heated ($T_e < 30$ eV) and under-ionized ($Z_{ave} < 10$). Notably, the 15-ns box-shaped (cases 1 and 2) and 36-ns Gaussian (cases 7 and 8) pulses, both operating at a comparable instantaneous power of approximately 5.1 MW at this evaluated timestamp, establish a favorable thermal balance. These configurations successfully elevate a substantial volume of the expanding corona into the 30–40 eV and $Z_{ave} \approx 10$–13 regime, providing the necessary thermodynamic conditions for maximizing in-band EUV emission.

The thermodynamic states established within the plasma directly dictate the transient generation and subsequent extraction of in-band EUV photons. Figure 5 shows the temporal evolution of the in-band EUV power for all eight cases. The temporal emission profiles rigorously reflect the ionization dynamics identified in the macroscopic plasma states. For the 15-ns Gaussian profiles, the in-band power exhibits a rapid onset followed by a rapid decline. This behavior is a direct consequence of rapid overheating; the high power injection quickly drives the localized electron temperature beyond the optimal regime, forcing the Sn ions into over-ionized states that cease to contribute to the 13.5-nm emission. In contrast, the 15-ns box-shaped profiles establish a broad, sustained emission plateau. This prolonged emission confirms that the constant energy injection rate effectively matches the hydrodynamic expansion timescale, thereby dynamically maintaining the expanding plasma volume within the optimal emitting temperature regime. The 36-ns box-shaped profiles generate a persistently low EUV output, which corroborates the severe underheating and insufficient ionization condition. The 36-ns Gaussian profiles yield a broad emission envelope with a high peak, indicating a favorable balance between the energy injection rate and expansion cooling over the extended pulse duration.

Furthermore, Fig. 5 reveals a systematic dependence of the extracted EUV power on the transverse spatial profile. Within each temporal waveform pairing, the configuration utilizing a spatial flat-top beam consistently generates higher instantaneous in-band power than its spatial Gaussian counterpart. As established in Figs. 3 and 4, the macroscopic absorbed energy and the overall multidimensional expansion morphology remain highly comparable between these spatial variants. Therefore, this substantial reduction in observable emission for the spatial Gaussian cases cannot be attributed to a deficit in primary energy coupling or a collapse of the emitting volume. Instead, the reduction must originate from severe localized radiation transport losses, specifically enhanced self-absorption within the plasma corona.

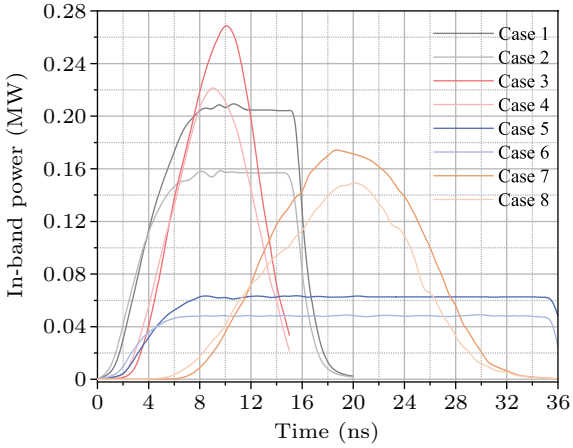


Fig. 5. Time-resolved in-band EUV emission power for the eight simulated spatiotemporal configurations. The in-band spectral window is defined as 13.5 nm ±1%. The line color and shading conventions correspond to the pairings defined in Fig. 3. The case numbers correspond to the irradiation conditions summarized in Table 1.

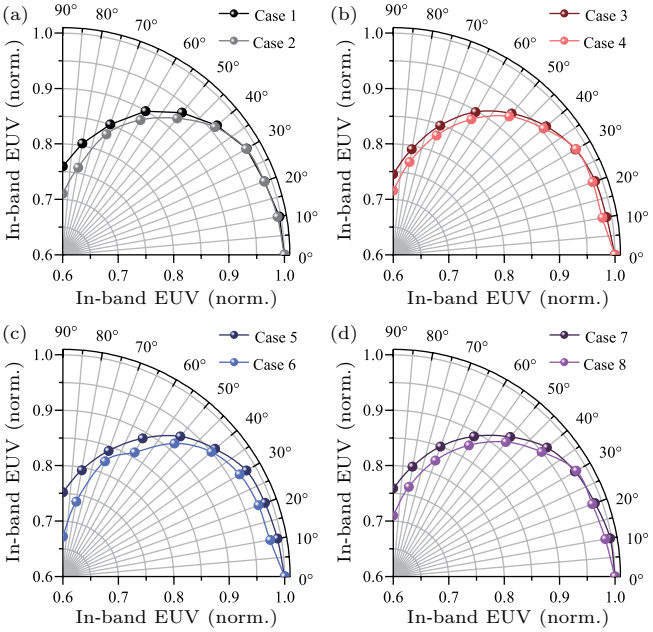


Fig. 6. Normalized angular distributions of the time-integrated in-band EUV energy for the eight spatiotemporal configurations. The observation angle is defined relative to the laser incidence axis (0°). To explicitly decouple the angle-dependent emission anisotropy from the absolute radiation yield, the angular distribution curve for each configuration is individually self-normalized to its respective maximum intensity along the laser incidence axis. The case numbers correspond to the irradiation conditions summarized in Table 1.

To explicitly isolate and evaluate this opacity mechanism, the angular distribution of the escaping EUV radiation is analyzed. Figure 6 presents the normalized time-integrated in-band EUV energy as a function of the observation angle. By self-normalizing each angular distribution curve to its respective on-axis (0°) maximum, the geometric isotropy of the EUV emission is distinctly decoupled from the absolute radiation yield. The data demonstrate that configurations driven by spatial Gaussian beams display a more forward-peaked angular distribution, characterized by a steeper attenuation of the normalized EUV intensity at larger observation angles (e.g., approaching 90°). Conversely, the spatial flat-top beams yield a broader, more isotropic emission profile.

This angle-dependent attenuation is fundamentally governed by the line-of-sight optical depth through the inhomogeneous plasma. EUV photons escaping at larger observation angles must geometrically traverse a significantly longer physical chord through the transverse periphery of the plasma corona. Under the evaluated overfill geometry, the extended, low-intensity radial wings of the spatial Gaussian beam deposit insufficient energy at the target periphery. This weak peripheral ablation creates a relatively cool, high-density, and under-ionized plasma shroud surrounding the hot emitting core. This peripheral shroud sustains a high photoabsorption cross section for 13.5-nm radiation, acting as a radial opacity barrier that severely attenuates high-angle photons. The spatial flat-top beam, providing uniform transverse irradiance and a sharp transverse truncation, uniformly ablates the target edge and suppresses the formation of this optically thick peripheral layer. By minimizing the extent of the cold peripheral plasma, the flat-top beam significantly reduces the line-of-sight optical depth at high angles, allowing a larger fraction of the internally generated EUV photons to escape across the entire collection solid angle.

The ultimate in-band CE represents the spatiotemporal integration of these transient generation and radiation transport processes. Figure 7 presents the overall CE for the eight configurations. The final CE systematically synthesizes the combined effects of the temporal heating balance and the spatial opacity mitigation. Within every temporal category, the spatial flat-top configuration definitively yields a higher CE than the corresponding spatial Gaussian configuration. Temporally, the 15-ns box-shaped pulse and the 36-ns Gaussian pulse achieve the highest efficiencies, as they provide an appropriate temporal power evolution to sustain the requisite ionization balance without inducing severe over-ionization or insufficient heating. Ultimately, case 1, which utilizes a 15-ns box-shaped temporal envelope and a 54-μm flat-top spatial profile, achieves the maximum CE of approximately 3.35%. This optimal performance demonstrates that maximizing the extraction of EUV radiation relies not merely on depositing total energy, but requires a rigorous dual-optimization strategy: temporal waveform shaping to sustain the intrinsic plasma emissivity, and spatial profile flattening to minimize angle-dependent opacity losses during photon transport.

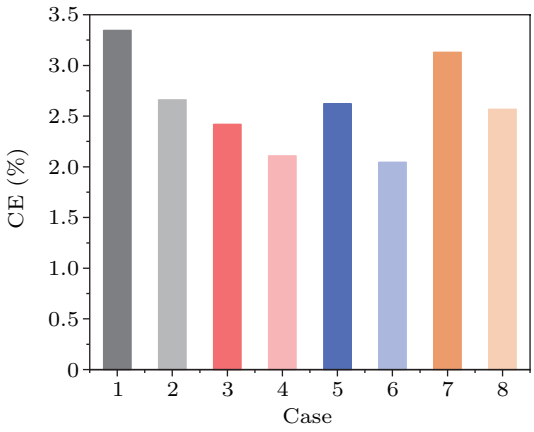


Fig. 7. Calculated total in-band CE for the eight simulated spatiotemporal configurations. The CE is evaluated according to the definition given in Section 2, using the fixed total incident single-pulse laser energy of 77 mJ. The case numbers correspond to the irradiation conditions summarized in Table 1.

To relate the present single-pulse spherical-droplet results to more practical EUV-source configurations, it is useful to consider their implications for preformed disk-like targets[3,31] generated in dual-pulse schemes. In industrially relevant source concepts, the main pulse typically irradiates an expanded Sn target rather than an initially spherical droplet. The present configuration is therefore not intended to reproduce the complete dual-pulse sequence, but to isolate the basic roles of

temporal and transverse pulse shaping under controlled energy and focusing conditions. Nevertheless, the physical mechanisms identified here are expected to provide useful guidance for preformed-target optimization. For a disk-like target, temporal waveform control should remain important because the main pulse must maintain a sufficiently large plasma volume within the favorable temperature and charge-state ranges for 13.5 nm emission while avoiding both local over-ionization and insufficient heating during hydrodynamic expansion. Similarly, transverse-profile control should remain important because the spatial distribution of deposited energy determines the peripheral density and temperature gradients, the formation of optically thick absorbing layers, and the angular escape of in-band photons. However, the exact optimal spatial profile may differ from that for a spherical droplet, since disk-like targets have a larger transverse extent and a different areal-density distribution. In such geometries, flat-top, annular, or other tailored profiles may be required to achieve homogeneous heating, favorable plasma confinement, and reduced radiation-transport losses. Therefore, the present results should be regarded as identifying general spatiotemporal design principles, while further simulations including realistic prepulse-induced target deformation will be necessary to determine the optimum conditions for practical dual-pulse EUV sources.

4. Summary

The optimization of laser-produced tin plasmas for extreme ultraviolet lithography necessitates precise control over multidimensional thermodynamic trajectories and radiation transport processes. In this study, we systematically decouple the effects of spatiotemporal laser pulse shaping on EUV emission from 4-μm-driven Sn microdroplets using radiation-hydrodynamics simulations. Initial wavelength-scaling evaluations confirm that the 4-μm driver operates within a macroscopic thermodynamic optimum, effectively balancing the inverse bremsstrahlung absorption efficiency against the line-of-sight optical depth of the expanding plasma. To isolate the underlying physical mechanisms, we construct a fully balanced $2 \times 2 \times 2$ parameter matrix varying pulse duration, temporal envelope, and transverse spatial profile. All simulations are rigorously constrained by an identical total single-pulse energy of 77 mJ and an industrially relevant overfill geometry, ensuring that subsequent variations in the plasma states and EUV yield are exclusively attributable to the spatiotemporal energy deposition gradients.

The comparative analysis reveals that temporal and spatial pulse shaping govern two distinctly decoupled aspects of EUV source physics. The temporal power injection rate acts as the primary mechanism regulating the instantaneous ionization balance. High-peak-power Gaussian pulses induce rapid transient overheating, driving the plasma into over-ionized states that deplete the EUV-emitting ion population and redirect absorbed energy into out-of-band transitions. Conversely, extended low-power continuous pulses fail to overcome hydrodynamic expansion cooling, resulting in under-heated and under-ionized plasmas. The implementation of moderate-power, box-shaped temporal profiles establishes a quasi-steady-state hydrodynamic regime. This dynamic balance effectively sustains a substantial plasma volume within the requisite 30–40 eV electron temperature window, thereby maximizing the intrinsic 13.5-nm emissivity throughout the pulse duration.

Concurrently, the transverse spatial profile dictates the efficiency of EUV photon extraction by modifying the line-of-sight optical depth. Under the evaluated overfill conditions, modifying the spatial intensity distribution from Gaussian to flat-top produces negligible variations in the total macroscopic absorbed energy and the geometric expansion of the critical density surface. However, angularly resolved emission data explicitly demonstrate that the extended low-intensity wings characteristic of a spatial Gaussian beam provide insufficient localized heating at the droplet periphery. This radial energy deficit facilitates the formation of a dense, under-ionized peripheral plasma shroud that exhibits high opacity to 13.5-nm radiation, severely attenuating photons escaping at large observation angles. The application of a spatial flat-top beam ensures uniform transverse irradiance, preventing the formation of this optically thick peripheral barrier and consequently promoting a more isotropic and efficient escape of the generated EUV photons.

Ultimately, the synthesis of these decoupled physical mechanisms determines the overall source efficiency. The configuration utilizing a 15-ns box-shaped temporal envelope combined with a 54-μm-radius spatial flat-top beam achieves the highest in-band CE of approximately 3.35%. These findings quantitatively establish that the theoretical advantages of the mid-infrared 4-μm drive wavelength can only be fully realized through a dual-optimization spatiotemporal strategy. Specifically, future EUV source engineering must independently implement temporal waveform synthesis to stabilize the intrinsic plasma ionization states and spatial beam homogenization to minimize localized radiation transport losses.

Acknowledgments

Project supported by the National Natural Science Foundation of China (Grant Nos. 12474279 and 12374384), Science Fund for Distinguished Young Scholars of Gansu Province (Grant No. 26JRRA016), Provincial-level Youth Talent Individual Project of Gansu Province (Grant

No. 2025QNGR15), and Youth Science and Technology Talent Innovation Project of Lanzhou City (Grant No. 2024-QN-200).

References

[1] Bakshi V 2018 *EUV Lithography* (2nd edn.) (Bellingham: SPIE Press)
[2] Banine V Y, Koshelev K N and Swinkels G H P M 2011 *J. Phys. D: Appl. Phys.* **44** 253001
[3] Versolato O O 2019 *Plasma Sources Sci. Technol.* **28** 083001
[4] Bakshi V 2023 *Photon sources for lithography and metrology* (Bellingham: SPIE Press)
[5] Wu B and Kumar A 2007 *J. Vac. Sci. Technol. B* **25** 1743
[6] Zhang X H, Wang W H, He C N, Yao Y C, Wang B Y, Li X H, Wang Z J, Qiu C, Sun H Y, Leng Y X and Xin G 2025 *Chin. Phys. B* **34** 114701
[7] Versolato O O, Sheil J, Witte S, Ubachs W and Hoekstra R 2022 *J. Opt.* **24** 054014
[8] Hemminga D J, Versolato O O and Sheil J 2023 *Phys. Plasmas* **30** 033301
[9] Schupp R, Torretti F, Meijer R A, Bayraktar M, Scheers J, Kurilovich D, Bayerle A, Eikema K S E, Witte S, Ubachs W, Hoekstra R and Versolato O O 2019 *Phys. Rev. Appl.* **12** 014010
[10] Mostafa Y, Behnke L, Engels D J, Bouza Z, Sheil J, Ubachs W and Versolato O O 2023 *Appl. Phys. Lett.* **123** 234101
[11] Mostafa Y, Behnke L, Engels D J and Versolato O O 2025 *J. Appl. Phys.* **138** 143304
[12] Pan Y, Tomita K, Sunahara A, Sasaki A and Nishihara K 2023 *Appl. Phys. Lett.* **123** 204103
[13] Hu Z, He L, Wang T, Lin N and Leng Y 2025 *Chinese Journal of Lasers* **52** 0601001 (in Chinese)
[14] Schupp R, Behnke L, Sheil J, Bouza Z, Bayraktar M, Ubachs W, Hoekstra R and Versolato O O 2021 *Phys. Rev. Res.* **3** 013294
[15] Shi Z Y, Yuan Y, Wang W P, Ma Y Y, Sun X Y, Lin N and Leng Y X 2023 *Phys. Plasmas* **30** 043107
[16] Behnke L, Schupp R, Bouza Z, Bayraktar M, Mazzotta Z, Meijer R, Sheil J, Witte S, Ubachs W, Hoekstra R and Versolato O O 2021 *Opt. Express* **29** 4475
[17] Schupp R, Torretti F, Meijer R A, Bayraktar M, Sheil J, Scheers J, Kurilovich D, Bayerle A, Schafgans A A, Purvis M, Eikema K S E, Witte S, Ubachs W, Hoekstra R and Versolato O O 2019 *Appl. Phys. Lett.* **115** 124101
[18] Dong Y L, Xu B H, Xiong W, Yang X H, Ma H H, Zhang G B, Wu Y T and Ma Y Y 2025 *Phys. Plasmas* **32** 123301
[19] Wang F F, Li J T, Sun X H, Yan B Z, Nie H K, Li X, Yang K J, Zhang B T and He J L 2022 *Chin. Opt. Lett.* **20** 011403
[20] Fujioka S, Nishimura H, Nishihara K, Sasaki A, Sunahara A, Okuno T, Ueda N, Ando T, Tao Y, Shimada Y, Hashimoto K, Yamaura M, Shigemori K, Nakai M, Nagai K, Norimatsu T, Nishikawa T, Miyanaga N, Izawa Y and Mima K 2005 *Phys. Rev. Lett.* **95** 235004
[21] White J, Dunne P, Hayden P, O'Reilly F and O'Sullivan G 2007 *Appl. Phys. Lett.* **90** 181502
[22] Ando T, Fujioka S, Nishimura H, Ueda N, Yasuda Y, Nagai K, Norimatsu T, Murakami M, Nishihara K, Miyanaga N, Izawa Y, Mima K and Sunahara A 2006 *Appl. Phys. Lett.* **89** 151501
[23] Tao Y, Harilal S S, Tillack M S, Sequoia K L, O'Shay B and Najmabadi F 2006 *Opt. Lett.* **31** 2492
[24] Sizyuk V, Sizyuk T and Hassanein A 2024 *J. Appl. Phys.* **135** 093101
[25] Dong Y L, Xu B H, Yang X H, Wu Y T, Xiong W, Zhang G B and Ma Y Y 2025 *Opt. Express* **33** 43894
[26] Min Q, Xu Z Y, He S Q, Lu H D, Liu X B, Shen R Z, Wu Y H, Pan Q K, Zhao C X, Chen F, Su M G and Dong C Z 2024 *Comput. Phys. Commun.* **302** 109242
[27] Min Q, Wang G D, He C W, He S Q, Lu H D, Liu X B, Wu Y H, Su M G and Dong C Z 2025 *Acta Phys. Sin.* **74** 033201 (in Chinese)
[28] He S Q, Min Q, Su M G, Lu H D, Wu Y H, Cao S Q, Sun D X, Zhang D H and Dong C Z 2023 *Opt. Express* **31** 7249
[29] He S Q, Min Q, Lu H D, Wu Y H, Cao S Q, Sun D X, Zhang D H, Su M G and Dong C Z 2024 *Opt. Lett.* **49** 566
[30] He S Q, Min Q, Wu Y H, Liu X B, He C W, Cao S Q, Pan Q K, Guo J, Chen F, Zhang D H, Su M G and Dong C Z 2024 *Opt. Express* **32** 17088
[31] Min Q, He C W, Lu H D, Liu X B, Su M G and Dong C Z 2025 *Phys. Rev. Res.* **7** 043155
[32] Su M G, Min Q, Cao S Q, Sun D X, Hayden P, O'Sullivan G and Dong C Z 2017 *Sci. Rep.* **7** 45212